OECD MCCI Project
Small-Scale Water Ingression and Crust Strength Tests (SSWICS)
SSWICS-8 Test Data Report: Thermal Hydraulic Results

Rev. 2 April, 2007

by:

S. Lomperski, M. T. Farmer, D. Kilsdonk, B. Aeschlimann

Nuclear Engineering Division
Argonne National Laboratory
9700 S. Cass Avenue
Argonne, IL 60439
USA

Table of Contents

List of Plots

1. Introduction

During the course of the first MCCI program, seven small-scale water ingression tests were performed with nominally 15 cm deep melt pools (up to 75 kg melt mass) made up of UO_2 and varying amounts of either siliceous or limestone common sand concrete. The concrete contents varied from a low of 4 wt% to a high of 23 wt%. These tests demonstrated that melt cooling can be enhanced by water ingression and that the role of water ingression increases with decreasing concrete content. The dependence of the water ingression cooling rate on concrete content is strongest for melts containing less than 14% concrete. For melts with 14% or more concrete, little evidence of water ingression cooling was discernible. It was also found that the cooling rates of the three high concrete content melts (two at 14% and one at 23%) were similar to one another.

One aim of this second MCCI program is to investigate the role of gas sparging on the corium cooling rate. The gases are a byproduct of the decomposition of concrete, which occurs when the material overheats. Gases generated near the corium/concrete interaction zone at the bottom of the melt are propelled up through the corium by buoyancy forces and the resultant gas flow has the potential to create melt porosity. This porosity is expected to supplement the fissures induced by thermal cracking. It is thought that these extra pathways will enhance the amount of water ingression cooling and quench the melt more rapidly than the case without sparging gases.

This first test of the current program is a small-scale water ingression test with the same SSWICS apparatus that was used for the prior seven tests, but adapted to provide gas injection during quench to simulate the flow of concrete decomposition gases. The corium composition and operating conditions duplicate that of SSWICS-6, a fully oxidized PWR corium melt containing 15 wt% siliceous concrete quenched at a system pressure of 1 bar. The data provides an opportunity to compare the cooling rate and crust morphology of corium quenched with and without sparging gases. The test, conducted on January 25, 2007, is designated SSWICS-8 and this report includes a description of the test apparatus, the instrumentation used, plots of the recorded data, and some rudimentary data reduction to obtain an estimate of the heat flux from the corium to the overlying water pool. A subsequent report will address post test measurements of crust composition, permeability, and mechanical strength.

2. System Description

2.1 Test Apparatus

The SSWICS reaction vessel (RV) has been designed to hold up to 100 kg of melt at an initial temperature of 2500^{o}C. The RV lower plenum consists of a 67.3 cm long, 45.7 cm (18") outer diameter carbon steel pipe (Fig. 2.1). The pipe is insulated from the melt by a 6.4 cm thick layer of cast MgO, which is called the "liner". The selected pipe and insulation dimensions result in a melt diameter of about 30 cm and a surface area of 707 cm^2. The melt depth at the maximum charge of 100 kg is about 20 cm.

The RV lower flange is insulated with a 6.4 cm thick slab of cast MgO (the "basemat") that spans the entire inner diameter of the pipe. The basemat and liner form the crucible

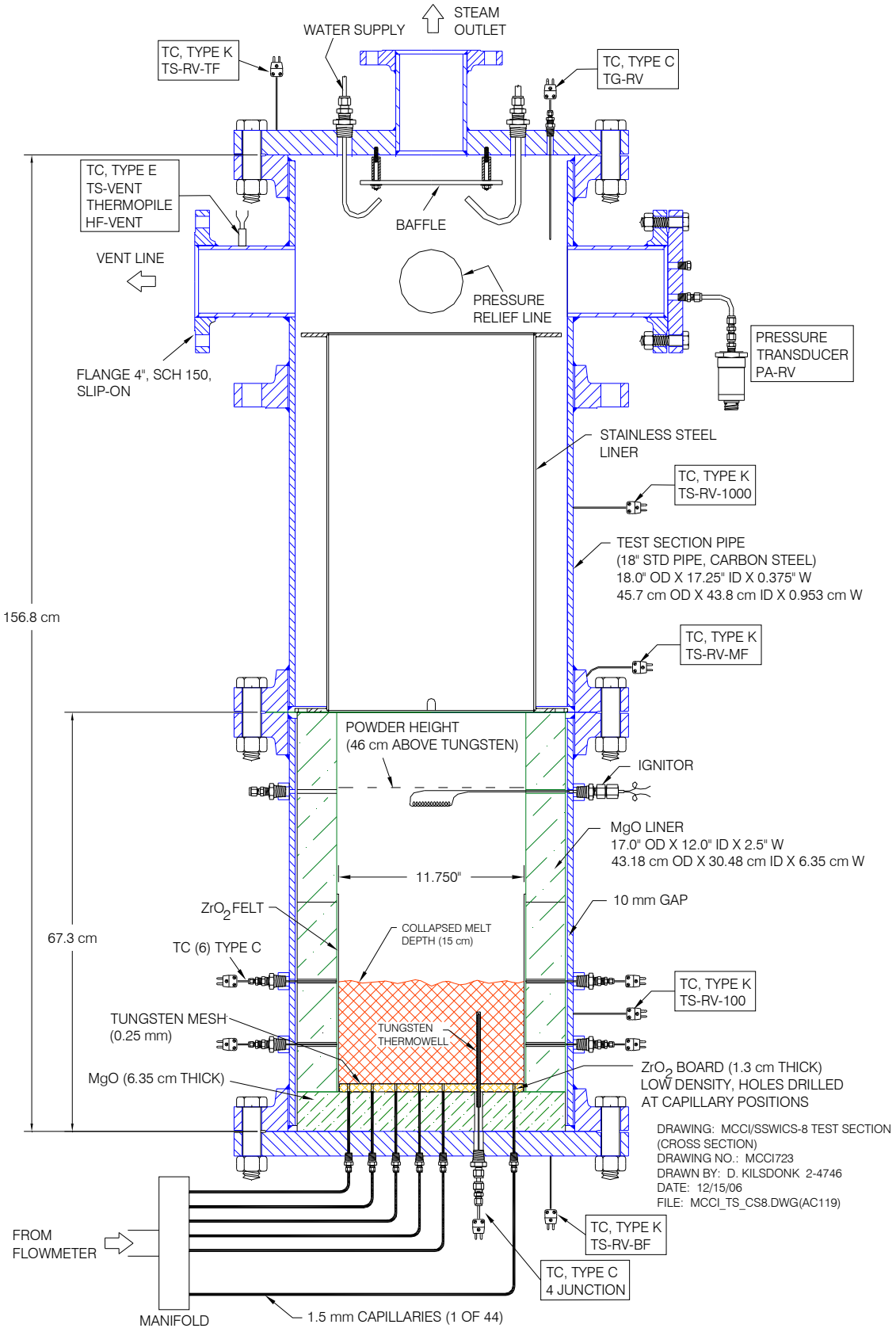

Figure 2.1 Side view of reaction vessel.

containing the corium. This particular geometry was chosen to facilitate removal of the basemat for the crust strength measurement tests. Corium has a tendency to bond with the MgO insulation and this design allows one to detach the basemat from the liner without damaging the crust.

The MgO slab is covered with a 1.3 cm thick, low density ZrO_2 board having a thermal conductivity ~1 W/m^{o}C. The purpose of this board is to protect the ends of the sparging system capillaries from the thermite during the ignition phase when the melt is at peak temperature. The melting point of stainless steel is ~1400^{o}C and the board must shield the capillaries from the >2000^{o}C thermite until heat losses to the crucible form a thin insulating crust of corium around the inside surface of the crucible. The board is rather fragile and can be eroded during thermite ignition, and so a tungsten mesh is placed over it as a mechanical barrier to slow the erosion rate. Small holes were drilled in the ZrO_2 board at each capillary location to ensure that there are gas paths directly upwards towards the melt even if the board is not completely eroded during thermite ignition.

The sparging gas is injected into the melt through forty four capillaries that are each 1.5 m long with 1.59 mm o.d. (1/16") and 0.57 mm i.d. On the upstream side, each capillary is connected to one of two plenums that are supplied with argon gas from a single flow controller. The downstream end of each capillary passes through the RV flange via a compression fitting and the tip is flush with the top of the MgO basemat as shown in Fig. 2.1.

The RV upper plenum consists of a second section of pipe with a stainless steel protective liner. Three 10 cm pipes welded near the top of the vessel provide 1) a vent line for the initial surge of hot noncondensable gases generated by the thermite reaction, 2) a pressure relief line with a rupture disk (7.7 bar at 100^{o}C), and 3) an instrument flange for the absolute pressure transmitter that measures the reaction vessel pressure. Four 6 mm (¼") tubes serve as water inlets for melt quenching. A baffle is mounted below the upper flange and the water flow is directed towards the baffle to reduce the momentum of the fluid before it drops down onto the melt. The baffle is also intended to prevent water droplets from being carried up towards the condenser, which would adversely affect the heat flux measurement. A fourth 10 cm pipe welded to the top flange provides an outlet to carry steam from the quenching melt to four cooling coils. The water-cooled coils condense the steam, which is collected within a 200 cm high, 20 cm diameter condensate tank (CT). Figure 2.2 is a schematic that provides an overview of the entire SSWICS melt-quench facility.

2.2 Instrumentation

Instrumentation has been selected to provide all measurements necessary to determine the melt dryout heat flux. Tables 2.1 and 2.2 list the sensors and major valves, respectively. The critical measurement for these tests is the steaming rate in the RV, which is found indirectly by measuring the rate of condensate collection in the CT. The condensate inventory is measured with a differential pressure sensor, PD-CT, and a time domain reflectometer, L-TDR-CT.

The remaining instrumentation provides supplementary information to further characterize the test conditions. The nomenclature used to identify thermocouples is as follows: TM (temperature within the corium melt), TF (fluid temperature), TG (gas space temperature),

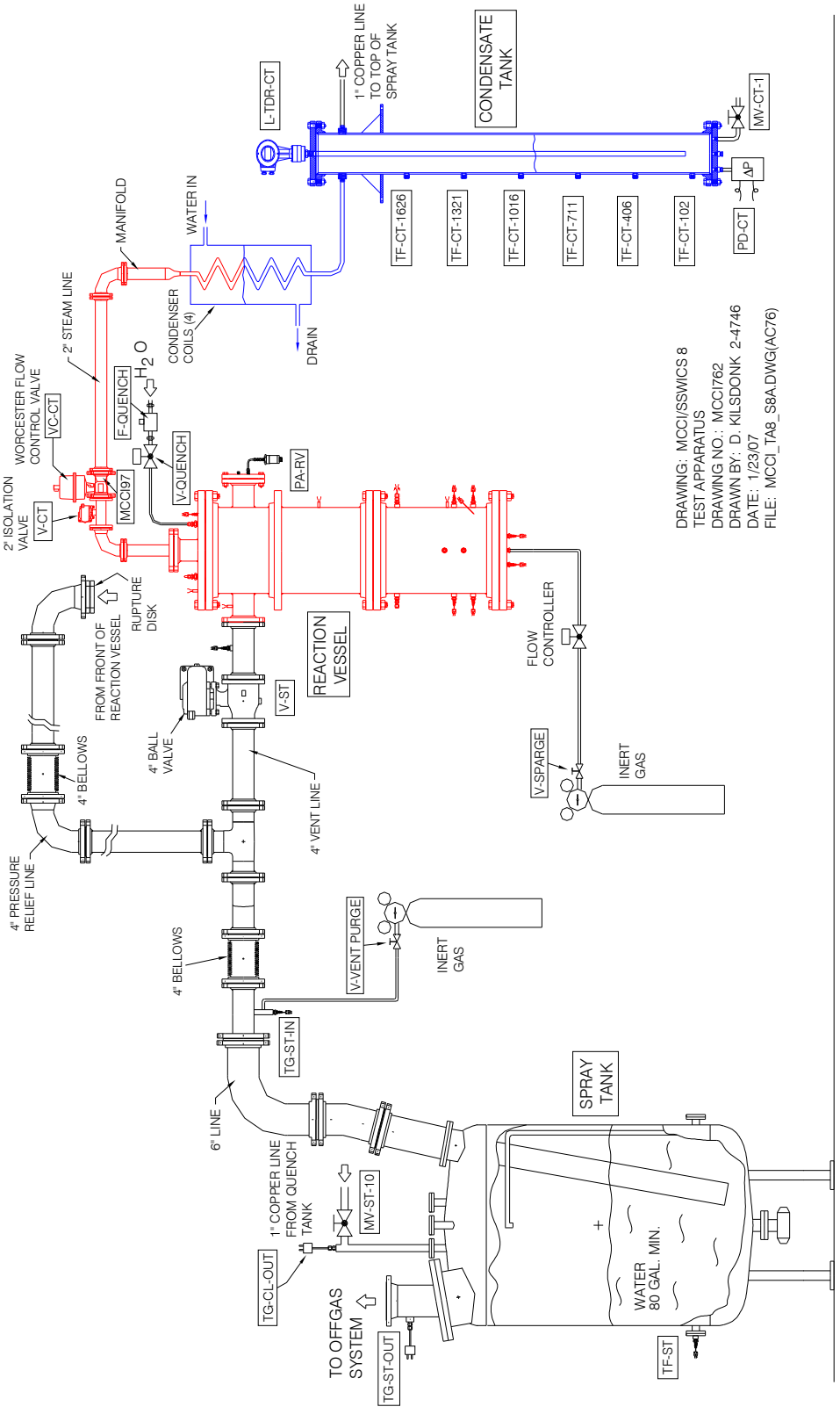

Figure 2.2 SSWICS melt quench facility.

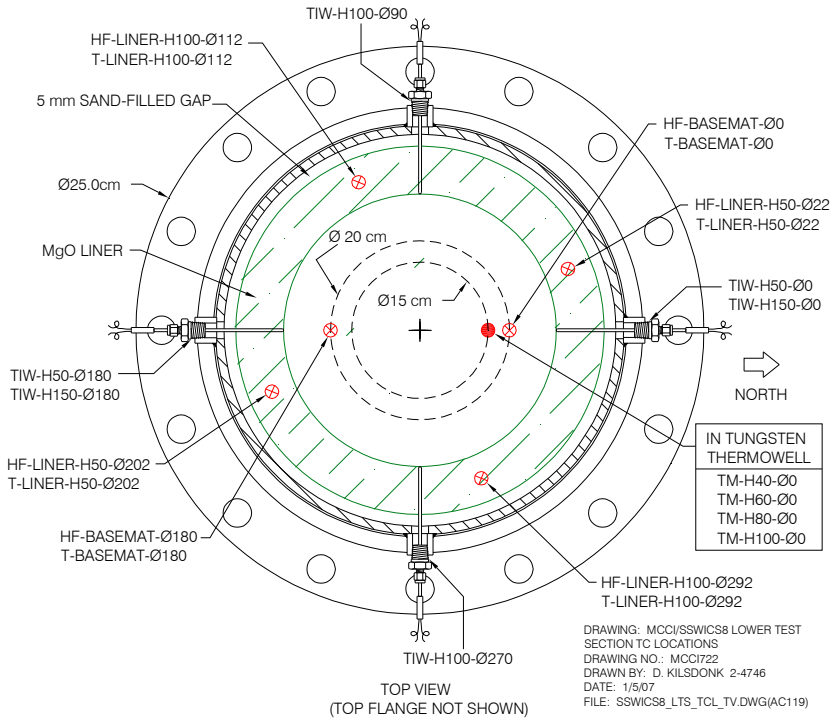

Figure 2.3 Heat flux and TC locations in the MgO crucible.

(height above the bottom of the melt, in mm, ϕ# (angle relative to direction north, in degrees). For example, TIW-H50-ϕ180 is located at the inner wall of the liner, 50 mm above the bottom of the melt and on the south side of the RV axis.

Six C-Type thermocouples with ⅛" diameter tantalum sheaths are used to measure temperatures at the inner surface of the liner (sensors labeled TIW in Fig. 2.3). They are mounted horizontally, passing through fittings in the RV wall and holes drilled through the liner. These sensors are used to detect the arrival of the quench front near the melt perimeter. Premature arrival of the front could indicate water seepage down along the liner and cooling of the melt from the side, which is undesirable. Though such seepage is deemed unlikely, this must be verified because the dryout heat flux measurement would be compromised by a melt that was partially cooled by water circumventing the crust. To measure melt temperatures, a 4-junction C-type thermocouple with ⅛" tantalum sheath is employed. The thermocouples are further protected with a tungsten thermowell (6 mm o.d., 150 mm long, 1 mm wall). The purpose of this sensor is to track the progress of the quench front down through the melt.

The gap between the liner and the RV wall (see Fig. 2.1) was filled with sand in an effort to reduce cooling of the liner and thus lateral heat losses. The concern has been that water can enter the gap and cool the outer surface of the liner through boiling, which would increase lateral heat losses beyond that expected for conduction cooling through the liner and RV wall with natural convection at the RV outer surface. Two new MgO liners were fabricated for this test

#	Channel	Name	Type	Description	Serial #	Output	Range	Accuracy
0	HPS-0	T-CJ-HPS	AD592 IC	Cold junction compensation sensor.	-	18 A/K	0-70°C	±0.5°C
1	HPS-1	TM-H100-Φ0	TC type C	Melt temp. 100 mm above bottom of melt (in tungsten thermowell).	-	0-37 mV	0-2320°C	±4.5°C or 1%
2	HPS-2	TM-H80-Φ0	TC type C	Melt temp. 80 mm above bottom of melt (in tungsten thermowell).	-	0-37 mV	0-2320°C	±4.5°C or 1%
3	HPS-3	TM-H60-Φ0	TC type C	Melt temp. 60 mm above bottom of melt (in tungsten thermowell).	-	0-37 mV	0-2320°C	±4.5°C or 1%
4	HPS-4	TM-H40-Φ0	TC type C	Melt temp. 40 mm above bottom of melt (in tungsten thermowell).	-	0-37 mV	0-2320°C	±4.5°C or 1%
5	HPS-5	Reserve	TC type C	-	-	0-37 mV	0-2320°C	±4.5°C or 1%
6	HPS-6	Reserve	TC type C	-	-	0-37 mV	0-2320°C	±4.5°C or 1%
7	HPS-7	Reserve	TC type C	-	-	0-37 mV	0-2320°C	±4.5°C or 1%
8	HPS-8	TIW-H50-Φ0	TC type C	Melt temp. at inner sidewall 50 mm above bottom of melt.	-	0-37 mV	0-2320°C	±4.5°C or 1%
9	HPS-9	TIW-H50-Φ180	TC type C	Melt temp. at inner sidewall 50 mm above bottom of melt.	-	0-37 mV	0-2320°C	±4.5°C or 1%
10	HPS-10	TIW-H100-Φ90	TC type C	Melt temp. at inner sidewall 100 mm above bottom of melt.	-	0-37 mV	0-2320°C	±4.5°C or 1%
11	HPS-11	TIW-H100-Φ270	TC type C	Melt temp. at inner sidewall 100 mm above bottom of melt.	-	0-37 mV	0-2320°C	±4.5°C or 1%
12	HPS-12	TIW-H150-Φ0	TC type C	Melt temp. at inner sidewall 150 mm above bottom of melt.	-	0-37 mV	0-2320°C	±4.5°C or 1%
13	HPS-13	TIW-H150-Φ180	TC type C	Melt temp. at inner sidewall 150 mm above bottom of melt.	-	0-37 mV	0-2320°C	±4.5°C or 1%
14	HPS-14	Reserve	TC type C	-	-	0-37 mV	0-2320°C	±4.5°C or 1%
15	HPS-15	Reserve	TC type C	-	-	0-37 mV	0-2320°C	±4.5°C or 1%
16	HPS-16	Reserve	TC type C	-	-	0-37 mV	0-2320°C	±4.5°C or 1%
17	HPS-17	Reserve	TC type C	-	-	0-37 mV	0-2320°C	±4.5°C or 1%
18	HPS-18	TG-RV	TC type C	Gas temp. in reaction vessel upper plenum.	-	0-37 mV	0-2320°C	±4.5°C or 1%
19	HPS-19	Reserve	TC type K	-	-	0-50 mV	0-1250°C	±2.2°C or 0.75%
20	HPS-20	Reserve	TC type K	-	-	0-50 mV	0-1250°C	±2.2°C or 0.75%
21	HPS-21	Reserve	TC type K	-	-	0-50 mV	0-1250°C	±2.2°C or 0.75%
22	HPS-22	TS-RV-tf	TC type K	Temperature of RV top flange.	-	0-50 mV	0-1250°C	±2.2°C or 0.75%
23	HPS-23	TS-RV-1000	TC type K	Outer wall temp. of RV 1000 mm above bottom of melt.	-	0-50 mV	0-1250°C	±2.2°C or 0.75%
24	HPS-24	TS-RV-mf	TC type K	Temperature of RV middle flange.	-	0-50 mV	0-1250°C	±2.2°C or 0.75%
25	HPS-25	TS-RV-100	TC type K	Outer wall temp. of RV 100 mm above bottom of melt.	-	0-50 mV	0-1250°C	±2.2°C or 0.75%
26	HPS-26	TS-RV-bf	TC type K	Temperature of RV bottom flange.	-	0-50 mV	0-1250°C	±2.2°C or 0.75%
27	HPS-27	TS-vent	TC type E	Outer wall temp. of vent line.	-	0-70 mV	0-900°C	±1.7°C or 0.5%
28	HPS-28	TF-CT-102	TC type K	Fluid temp. in condensate tank at a water level of 102 mm.	-	0-50 mV	0-1250°C	±2.2°C or 0.75%
29	HPS-29	TF-CT-406	TC type K	Fluid temp. in condensate tank at a water level of 406 mm.	-	0-50 mV	0-1250°C	±2.2°C or 0.75%
30	HPS-30	TF-CT-711	TC type K	Fluid temp. in condensate tank at a water level of 711 mm.	-	0-50 mV	0-1250°C	±2.2°C or 0.75%
31	HPS-31	TF-CT-1016	TC type K	Fluid temp. in condensate tank at a water level of 1016 mm.	-	0-50 mV	0-1250°C	±2.2°C or 0.75%
32	HPS-32	TF-CT-1321	TC type K	Fluid temp. in condensate tank at a water level of 1321 mm.	-	0-50 mV	0-1250°C	±2.2°C or 0.75%
33	HPS-33	TF-CT-1626	TC type K	Fluid temp. in condensate tank at a water level of 1626 mm.	-	0-50 mV	0-1250°C	±2.2°C or 0.75%
34	HPS-34	TF-HX-in	TC type K	Fluid temp. at HX coolant inlet.	-	0-50 mV	0-1250°C	±2.2°C or 0.75%
35	HPS-35	TF-HX-out	TC type K	Fluid temp. at HX coolant outlet.	-	0-50 mV	0-1250°C	±2.2°C or 0.75%

Table 2.1 Instrumentation list (part 1 of 2).

#	Channel	Name	Type	Description	Serial #	Output	Range	Accuracy
36	HPS-36	HF-vent	Thermopile	Heat Flux through connecting line to V-ST.	0632	0-5.50 mV	0-5 kW/m^2	±3%
37	HPS-37	I-ign	DC supply	Current supply for thermite ignitor.	-	0-100 mV	0-25 Amps	-
38	HPS-38	TF-quench	TC type K	Temperature of water injected into RV	-	0-50 mV	0-1250^{o}C	±2.2^{o}C or 0.75%
39	HPS-39	Reserve	-	-	-	-	-	-
40	HPS-40	PA-RV	1810AZ	Absolute pressure in reaction vessel.	02351-00P1PM	1-6 V	0-14 bar gage	±0.14 bar
41	HPS-41	PD-CT	1801DZ	8P transmitter to measure condensate inventory.	D-9	0-13 V	0-0.35 bar	±0.004 bar
42	HPS-42	L-TDR-CT	BM100A	Time domain reflectometer to measure CT level.	A02331879A	4 - 20 mA	0 - 2 m	±3 mm
43	HPS-43	VDC-P-supply	-	Voltage of the power supply for the pressure transmitters.	-	0 - 15 V	-	-
44	HPS-44	F-sparge	HFC-203	Flow rate of argon into injector for gas sparging	3621300001	0 - 5 V	0-50 sl/m Ar	±0.5 sl/m
45	HPS-45	Reserve	-	-	-	-	-	-
46	HPS-46	Reserve	-	-	-	-	-	-
47	HPS-47	Reserve	-	-	-	-	-	-
48	HPS-48	HF-liner-H50-Φ22	Thermopile	Radial heat flux through liner, 50 mm above bottom of melt.	403	0-40 mV	0-3 MW/m^2	±5%
49	HPS-49	HF-liner-H50-Φ202	Thermopile	Radial heat flux through liner, 50 mm above bottom of melt.	402	0-40 mV	0-3 MW/m^2	±5%
50	HPS-50	HF-liner-H100-Φ112	Thermopile	Radial heat flux through liner, 100 mm above bottom of melt.	404	0-40 mV	0-3 MW/m^2	±5%
51	HPS-51	HF-liner-H100-Φ292	Thermopile	Radial heat flux through liner, 100 mm above bottom of melt.	405	0-40 mV	0-3 MW/m^2	±5%
52	HPS-52	HF-basemat-Φ0	Thermopile	Heat flux through basemat, 20 mm from axial center of melt.	406	0-40 mV	0-3 MW/m^2	±5%
53	HPS-53	HF-basemat-Φ180	Thermopile	Heat flux through basemat, 20 mm from axial center of melt.	401	0-40 mV	0-3 MW/m^2	±5%
54	HPS-54	T-liner-H50-Φ22	TC type K	Liner temp. at heat flux meter, 50 mm above bottom of melt	403	0-50 mV	0-1250^{o}C	±2.2^{o}C or 0.75%
55	HPS-55	T-liner-H50-Φ202	TC type K	Liner temp. at heat flux meter, 50 mm above bottom of melt	402	0-50 mV	0-1250^{o}C	±2.2^{o}C or 0.75%
56	HPS-56	T-liner-H100-Φ112	TC type K	Liner temp. at heat flux meter, 100 mm above bottom of melt	404	0-50 mV	0-1250^{o}C	±2.2^{o}C or 0.75%
57	HPS-57	T-liner-H100-Φ292	TC type K	Liner temp. at heat flux meter, 100 mm above bottom of melt	405	0-50 mV	0-1250^{o}C	±2.2^{o}C or 0.75%
58	HPS-58	T-basemat-Φ0	TC type K	Basemat temperature at heat flux meter.	406	0-50 mV	0-1250^{o}C	±2.2^{o}C or 0.75%
59	HPS-59	T-basemat-Φ180	TC type K	Basemat temperature at heat flux meter.	401	0-50 mV	0-1250^{o}C	±2.2^{o}C or 0.75%
60	HPQ-50	T-CJ-HPQ	AD592 IC	Cold junction compensation sensor.	-	18A/K	0-70^{o}C	±0.5^{o}C
61	HPQ-51	TF-ST	TC type K	Fluid temp. in spray tank.	-	0-50 mV	0-1250^{o}C	±2.2^{o}C or 0.75%
62	HPQ-52	TG-CL-out	TC type K	Gas temperature in condensate tank outlet line to spray tank.	-	0-50 mV	0-1250^{o}C	±2.2^{o}C or 0.75%
63	HPQ-53	TG-ST-in	TC type K	Gas temp. in the spray tank line inlet.	-	0-50 mV	0-1250^{o}C	±2.2^{o}C or 0.75%
64	HPQ-54	TG-ST-out	TC type K	Gas temp. in the spray tank line outlet.	-	0-50 mV	0-1250^{o}C	±2.2^{o}C or 0.75%
65	HPQ-55	F-quench	Paddlewheel	Flow rate of water into reaction vessel (for quenching melt).	3144	0-5 V	0-50 gpm	±0.5 gpm
66	HPQ-56	F-HX	Paddlewheel	Flow rate of cold water to heat exchangers.	3143	0-5 V	0-50 gpm	±0.5 gpm

Table 2.2 Instrumentation list (part 2 of 2).

Table 2.3 Remotely operated valves.

Channel #		Valve Name	Type	Description	Actuator
1		V-CT	Ball valve	Valve on steam line between reaction vessel and quench tank.	Pneumatic
2		V-quench	Ball valve	Valve on quench water supply line into reaction vessel.	Solenoid
3		V-quench-i	Ball valve	Isolation valve on quench water supply line into reaction vessel.	Solenoid
4		V-quench-b	Ball valve	Valve on back-up quench water supply.	Solenoid
5		V-ST	Ball valve	Valve on vent line between reaction vessel and spray tank.	Pneumatic
-		V-HX	Ball valve	Valve on cooling-water line to heat exchangers.	Solenoid
-		VC-CT	Ball valve	Control valve on steam line between reaction vessel and quench tank.	Electric

and they provide a very close fit with the RV. The gap between the RV wall and liner is no more than 2-3 mm at its widest points.

The entire RV was insulated from the top of the melt level upwards. The lower 25 cm of the RV was left uninsulated so that any excessive wall heating or corium breach could be readily observed.

3. Test Parameters and Course of Test

The specifications for this test are listed in Table 3.1 along with those of the first seven tests for comparison. The measured masses of the constituents of the corium powder charge are listed in Table 3.2. The 68 kg charge was selected to produce an approximate melt depth of 15 cm. The test was conducted on January 25, 2007.

The facility was preheated to bring the structure temperatures up to about 100°C. During this period the water used for melt quenching was preheated to about 95°C. The preheating is used to reduce the amount of energy absorbed by heat sinks in the early stages of the test. This maximizes the amount of steam reaching the heat exchanger and reduces corrections to the measured corium heat flux. It takes roughly 2 hours for the RV structures to reach 100°C.

Argon was used as the sparging gas and the flow rate directed for the test is 11 slpm (standard liters/minute; corresponds to a superficial gas velocity of 2 cm/s at a temperature of 2000°C). The flow controller is located within the cell and cannot be adjusted from the control room. Therefore the gas flow was initiated at the same time as the RV structure preheat since the cell is inaccessible once the preheat phase has begun. The gas flow at the moment of thermite ignition, and for the remainder of the test, was 11 slpm.

The igniter coil was energized to initiate thermite ignition, which was first detected by a sudden rise in the upper plenum gas temperature TG-RV. Thermocouples within the melt began rising about thirty seconds later. The melt thermocouples within the thermowell (TM-H100-ϕ0 through TM-H40-ϕ0) rose rapidly to an initial peak temperature of about 1900°C and then began to slowly fall. Figure A.1 shows the first thirty minutes of the transient (all plots are attached as an appendix). All data has been plotted so that the x-axis origin corresponds with the initial rise in TG-RV.

The next phase of the experiment was the initial quench of the melt. Valve V-CT was opened 48 s after ignition so that steam would be able to travel to the heat exchangers. At the same time, valve V-ST was closed to isolate the vent line and spray tank from the system. Water injection was initiated at 99 s at an average flow rate of 10 l/min, lasting for 4 minutes (ending at 350 s) and resulting in an integrated flow of approximately 40 liters. The system pressure, which had briefly peaked near 1.5 bar near the beginning of the injection phase, soon settled near 1 bar and remained there for the rest of the test.

The test continued until all melt temperatures had reached the saturation temperature of 100°C, which occurred at an elapsed time of ~15000 s.

Table 3.1 Test specifications for completed SSWICS experiments.

Parameter	Test Number							
	1	**2**	**3**	**4**	**5**	**6**	**7**	**8**
Melt composition (wt% $UO_2/ZrO_2/Cr$/Concrete)	61/25/6/8	61/25/6/8	61/25/6/8	48/20/9/23	56/23/7/14	56/23/6/14	64/26/6/4	56/23/6/14
Concrete type	LCS	SIL	LCS	LCS	LCS	SIL	LCS	SIL
Melt mass (kg)	75	75	75	60	68	68	80	68
Melt depth (cm)	15	15	15	15	15	15	15	15
Initial Melt Temperature (^oC)	~2300	~2100	~2100	~2100	~2100	~1950	~2100	~1900
System pressure (bar)	1	1	4	4	4	1	4	1
Water injection flowrate (lpm)	4	4	12	13	6	14	13	10
Water injected (liters)	33	39	34	40	61	47	40	41
Test date (day/mo/year	30/08/02	17/09/02	30/01/03	13/03/03	15/10/03	24/02/04	14/12/04	25/01/07

Constituent	Mass (kg)
U_3O_8	39.92
CrO_3	8.40
CaO	1.50
Zr	11.68
Mg	0.04
Si	1.08
SiO_2	5.32
Al	0.06
Total	68.0

Tables 3.2 Corium powder charge and reaction product mass fractions.

Constituent	Wt %	
	Reactant	Product
U_3O_8	58.70	-
UO_2	-	56.32
Zr	17.16	-
ZrO_2	-	23.13
Si	1.57	-
SiO_2	7.84	11.17
Mg	0.07	-
MgO	-	0.12
Al	0.09	-
Al_2O_3	-	0.64
CaO	2.21	2.21
CrO_3	12.36	-
Cr	-	6.41

4. Sensor Malfunctions and Abnormalities

Post test examination of the test apparatus and a preliminary review of the data indicate the following:

1) The signal from sensor TM-H100-ϕ0 began to fail around 9700 s, recovered near 10500 s, then permanently failed near 10900 s.
2) The electrical connections to the basemat heat flux meters and TCs were damaged during assembly and unavailable for the test (HF-basemat-ϕ0, HF-basemat-ϕ180, T-basemat-ϕ0, T-basemat-ϕ180). The cabling of a TC associated with a liner heat flux meter was also damaged (T-liner-H100-ϕ112). The damage was caused by the unusually tight fit between the newly cast MgO liners and the RV wall, which left very little room to bring the wires to the Conax fittings.

5. Data Reduction

Some simple calculations have been performed to provide a preliminary assessment of the test data. The first is a calculation of the coolant inventory in the RV as a function of time. The inventory is the difference between the total amount of liquid injected and the amount boiled off and collected in the CT:

$$M_{H_2O-RV} = \sum_{t=0}^{t=t_{end}} \rho \dot{V} \Delta t \quad - \quad \frac{\pi}{4} D^2 \frac{\Delta P}{g} \tag{5.1}$$

where data from sensor F-quench is used for the volumetric flow rate $\dot{V}$ and the liquid density ρ is taken to be 998 kg/m^3. The condensate inventory is calculated with readings from sensor PD-CT (ΔP) and the tank diameter D of 0.203 m. Figure A.9 shows both the integrated mass flow and CT inventory, labeled F-integrated and M-CT, respectively. The calculated net coolant inventory, denoted M-RV, confirms that the corium was always covered with water.

The corium heat flux was calculated using two different methods. The first considers the rate of condensate collection, which is a measure of the steam flow rate from the RV. Accurate determination of the heat flux at the corium surface must, however, account for various heat sinks. During the injection phase, energy is absorbed raising the coolant to the saturation temperature. Some of the vapor produced by the quenching melt condenses on the walls of the upper plenum to heat the RV structures to the saturation temperature. Later, heat losses from the upper plenum generate continued condensation. Accounting for these heat sinks, the rate of energy transfer through the corium surface is written as:

$$Q = M_{RV}\, c_p \frac{\partial T}{\partial t} + \dot{m}\, h_{fg} + \left[M_S c_M \frac{\partial T}{\partial t} + Q_{HL} \right] \Bigg|_{up} \tag{5.2}$$

where $\dot{m}$ is mass flow rate of condensate into the CT, M_S is the mass of the RV upper plenum structures, c_M is their heat capacity,, and Q_{HL} represents total upper plenum heat losses. For this report, liquid subcooling has been neglected (an accurate assumption after the injection phase) along with heat losses and time variations in structure temperatures. The condensation rate is calculated from the time derivative of the differential pressure signal PD-CT. The heat transfer rate from the corium is then:

$$Q = \frac{1}{g} \frac{\pi}{4} D^2 \frac{\partial \Delta P}{\partial t} h_{fg} \tag{5.3}$$

where D is again the inner diameter of the CT and the heat of vaporization h_{fg} is 2130 kJ/kg^{o}C (TG-RV registered 100^{o}C through most of the transient). The heat flux is obtained by scaling Q with the initial surface area of the corium (0.071 m^2). The derivative was calculated with pairs of averaged ΔP readings (an average of 5 measurements at 0.5 Hz) centered around a Δt of 60 s. The averaging and length of Δt were necessary to reduce oscillations in the calculated heat flux.

The second method of calculating corium heat flux uses an energy balance on the secondary side of the heat exchanger. The measured parameters are the coolant flow rate on the secondary side of the cooling coils and the inlet and outlet coolant temperatures. The cooling power of the heat exchanger is then:

$$Q_{HX} = \rho \dot{V}_{HX}\, c_p (T_{out} - T_{in}) \tag{5.4}$$

where readings from sensors TF-HX-in and TF-HX-out were used for temperatures T_{in} and T_{out}, respectively. Data from the flow meter F-HX was used for $\dot{V}_{HX}$ while the density and heat capacity of water were taken to be 982 kg/m^3 and 4.18 kJ/kg^{o}C, respectively.

The cooling power of the heat exchanger is related to the steam flow rate out of the RV by the following:

$$Q_{HX} = \dot{m}\,[h_{fg} + c_p (T_{sat} - T_{con})] \tag{5.5}$$

where $\dot{m}$ is the mass flow rate of steam into the heat exchanger (identical to the flow rate of condensate into the CT, as defined in equation 5.2). From equation 5.5 it can be seen that if condensate leaves the heat exchanger at the saturation temperature, i.e., there is no subcooling, the cooling power of the heat exchanger is equal to the product of $\dot{m}$ and h_{fg}. In this case, according to equation 5.2, the cooling power of the heat exchanger equals the heat transfer rate from the melt. However, the condensate does not, in general, leave the heat exchanger at the saturation temperature. The result of this subcooling is an overestimation of the corium heat flux when using equation 5.5 and the assumption of $T_{sat} = T_{con}$ (as plotted in Fig. A.14).

The corium heat flux could be calculated more accurately with the heat exchanger energy balance through the addition of a condensate temperature measurement at the heat exchanger outlet. However, the calculation would still require the steam mass flow rate, which would be derived from the CT level measurements. Thus the heat exchanger energy balance, with the assumption of $T_{sat} = T_{con}$, is considered to be a rough check of the heat flux measurements derived directly from the CT level measurements using equation 5.3.

6. Post Test Assessment of Injection System Performance

The main goal of Test 8 is to assess the influence of gas injection on the melt cooling rate. A preliminary cross comparison has been made of data from Tests 6 & 8 (same melt composition and quench conditions) to obtain an initial indication of the influence of the gas. The two tests can be compared by plotting the melt temperatures versus time (Fig. A.15) and the calculated heat flux versus time (Fig. A.16). From these plots it can be seen that Test 8 data is very similar to Test 6 data (Test 7, a melt with less concrete, is an example of a test with a much different cooling rate). These curves suggest that the corium cooling rate was unaffected by the gas injection.

It is instructive to examine the physical condition of the quenched corium and so photos of the top and bottom are provided in Figs. A.17 & 18. The photos show a nearly solid, though cracked piece of corium that looks much like the one produced in Test 6. The sole notable difference is the volcanic structure on top of the ingot (~48 mm high and ~95 mm diameter), which could have been generated early in the test by the flow of gas. No such structure formed on any of the other ingots. This suggests that gas did indeed flow up through the corium early in the test while most of the sample was molten.

The cooling rates for Tests 6 & 8 are similar, but post test examinations of the ingot give rise to uncertainty in the actual path taken by the injected gas over the course of the test. The post test exams consisted of the following:

1) The capillaries within the basemat were examined for signs of blockage. Each capillary was connected to an argon supply and individually tested. Several tubes were partially blocked and one completely blocked, but nearly all were clear. This confirms that during Test 8 the argon flow was distributed across the bottom of the corium as designed.
2) The ingot was placed back on top of the basemat in an attempt to recreate the flow conditions that existed during the test. Since the entire assembly was outside the reaction vessel, the flow path taken by the gas could be observed directly. The actual test conditions could not, of course, be faithfully reproduced because the seal between the basemat and liner was broken when the ingot was first removed from the basemat for cleaning, inspection, and photos. There is also a large difference between the quench test corium/MgO temperature and the post test temperature.
3) The basemat could not be properly resealed to the liner with zirconia cement because of corium protrusions and rough surfaces on the underside of the ingot. Rather than chip away the corium with the hope of recreating a ceramic seal similar to the old one, the joint was sealed instead with RTV. It is believed that at room temperature an RTV seal is superior to that of the zirconia cement.
4) The basemat seal was tested by pouring water over the ingot. Water leakage through the RTV seal occurred even with a small water head (~1 cm deep pool). Since we failed to seal the joint with RTV at room temperature, it is considered unlikely that this joint was tight with zirconia cement.
5) There was also water leakage through the side holes where the thermocouples were once located. Though these holes were blocked by the TCs during the test, they were sealed with zirconia cement and so they might also have leaked during the test.
6) All capillaries were reconnected to the manifold and an 11 lpm argon flow through the injection system established. Water was poured into the liner until there was a shallow pool over the corium. None of the gas bubbled up through the corium. Instead, gas leaked through the basemat joint and the side holes.

Conclusion:

The gas injection system itself functioned as designed, but once there was a layer of solid corium immediately above the capillaries, the gas probably traveled around the corium pool rather than through it. It is possible that during the very early stages of the test, while nearly all the corium was molten, gas traveled straight up through the melt as planned. This would explain the existence of the volcanic structure. A crust subsequently forms along the relatively cold surfaces of the MgO basemat and liner. The crust is permanent and grows with time because there is no corium heating in these SSWICS tests. This initial crust may present an early barrier to gas flow up through the corium. There appear to be two main pathways for gas bypass, 1) through the basemat joint and 2) up between the corium/liner interface and out through the side holes. On

the basis of our post test examinations it would be reasonable to conclude that most or all of the gas travels around the corium soon after the crust is formed. This leads us to conclude that the operating conditions for Tests 6 & 8 were effectively the same and that Test 8 provides little information on the effects of gas sparging on melt cooling rate. A final determination will be made after the ingot is sectioned for load testing.

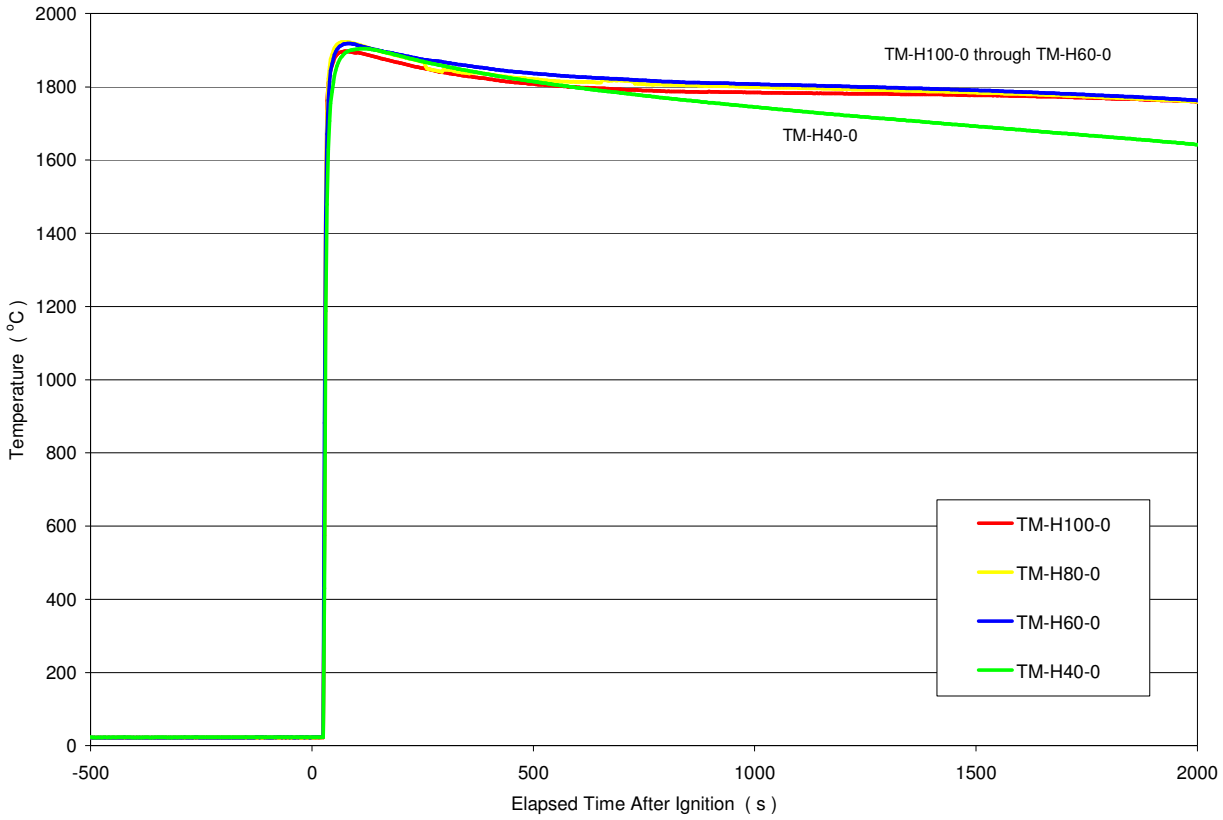

Figure A.1 Melt temperatures early in the transient (TCs inside tungsten thermowell).
Figure A.2 Melt temperatures for the entire test duration.

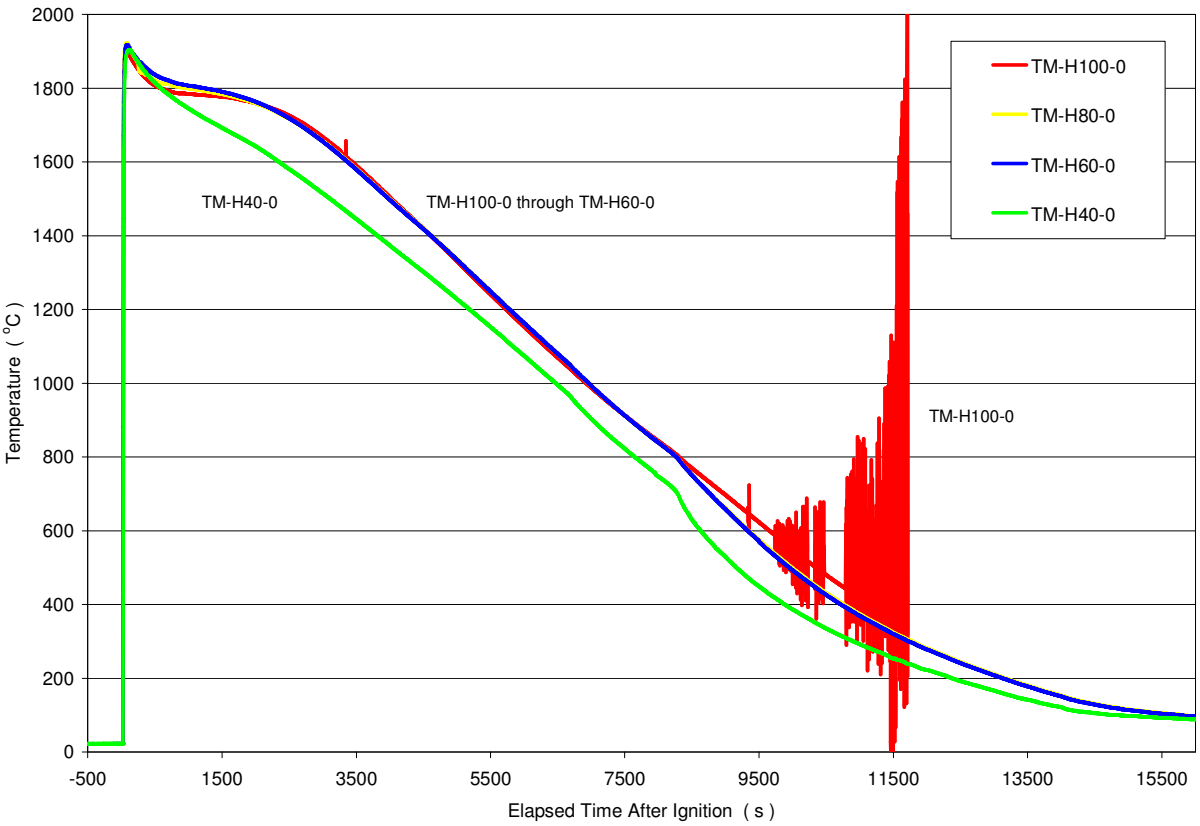

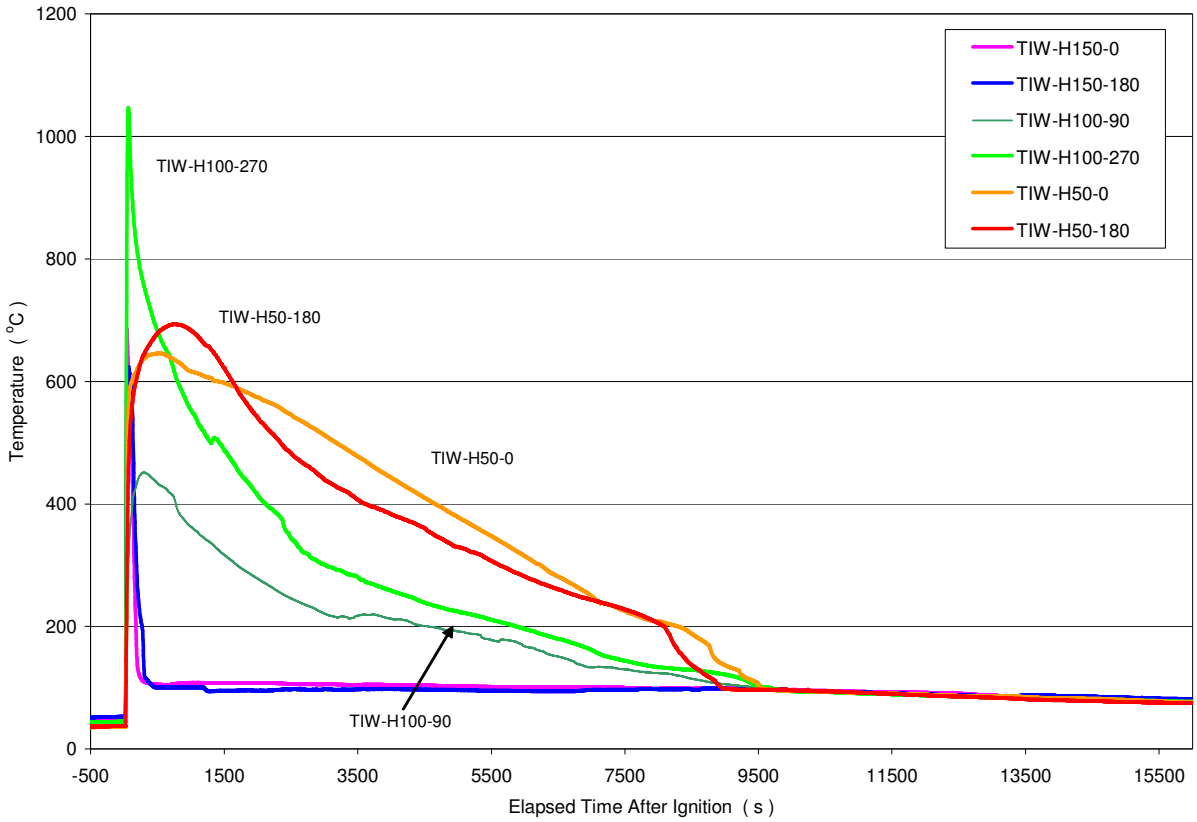

Figure A.3 Temperatures at the inner wall of MgO liner.

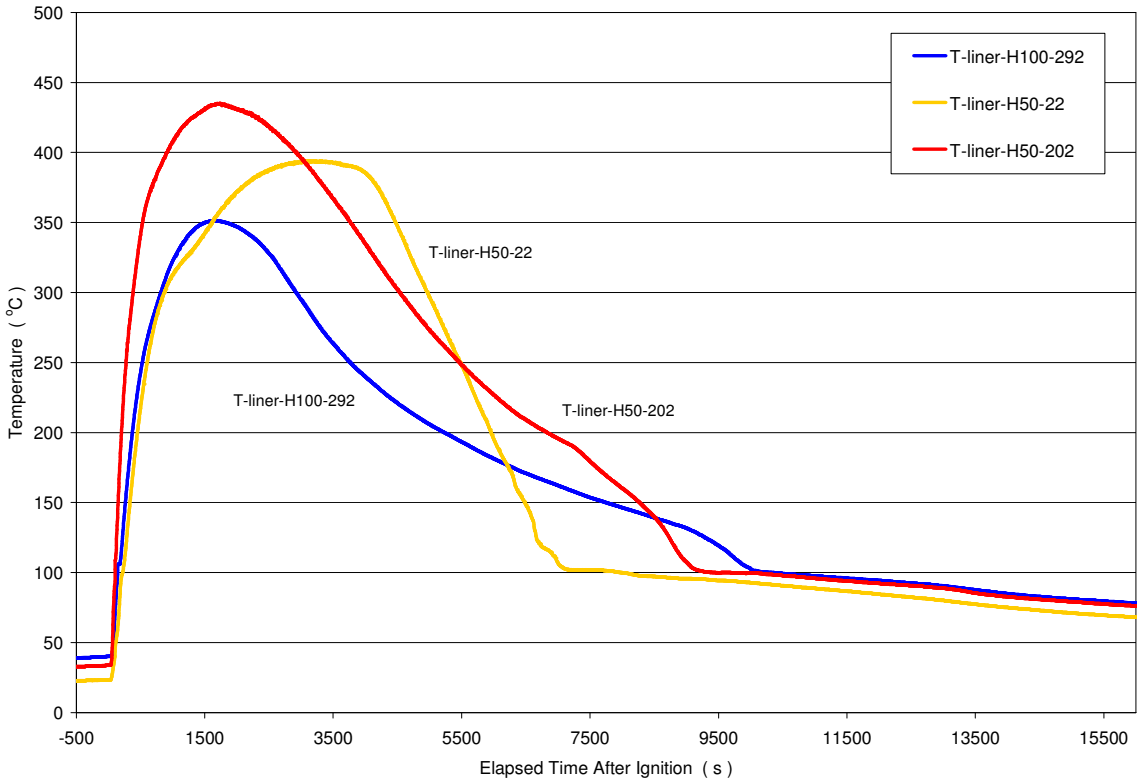

Figure A.4 Temperature of MgO liner at heat flux meter locations.

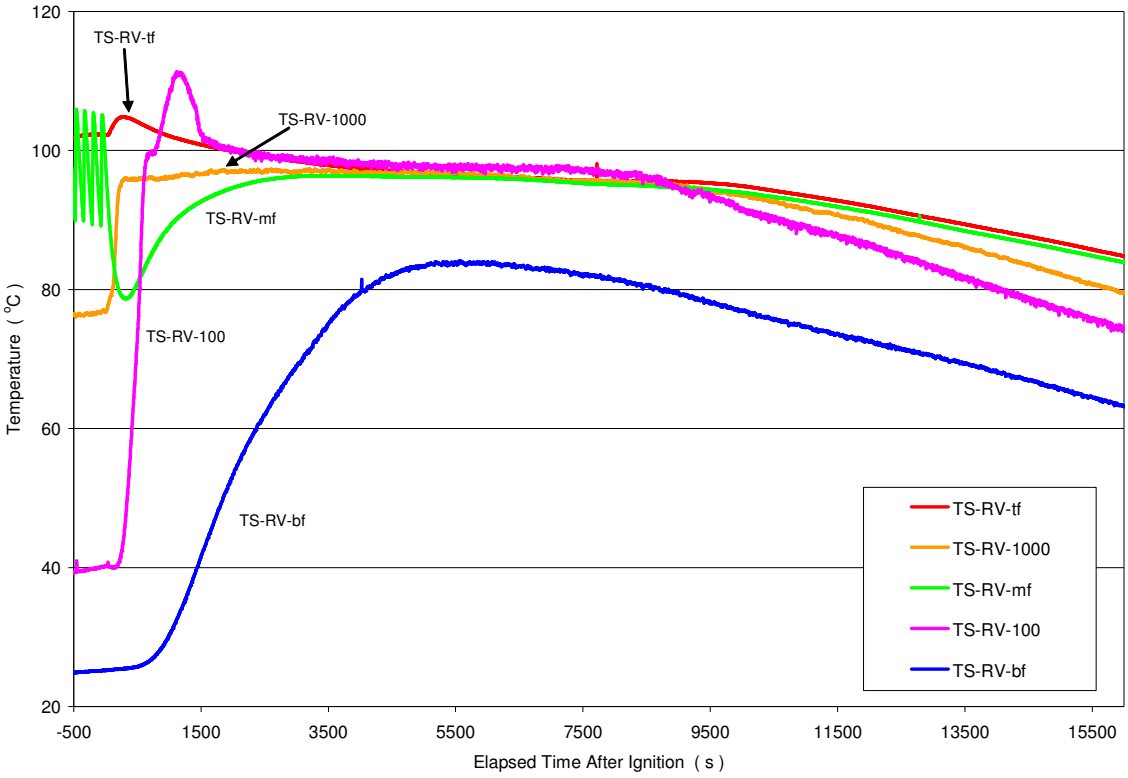

Figure A.5 Temperatures of steel structures.

Figure A.6 Total pressure in reaction vessel and position of valve V-quench.

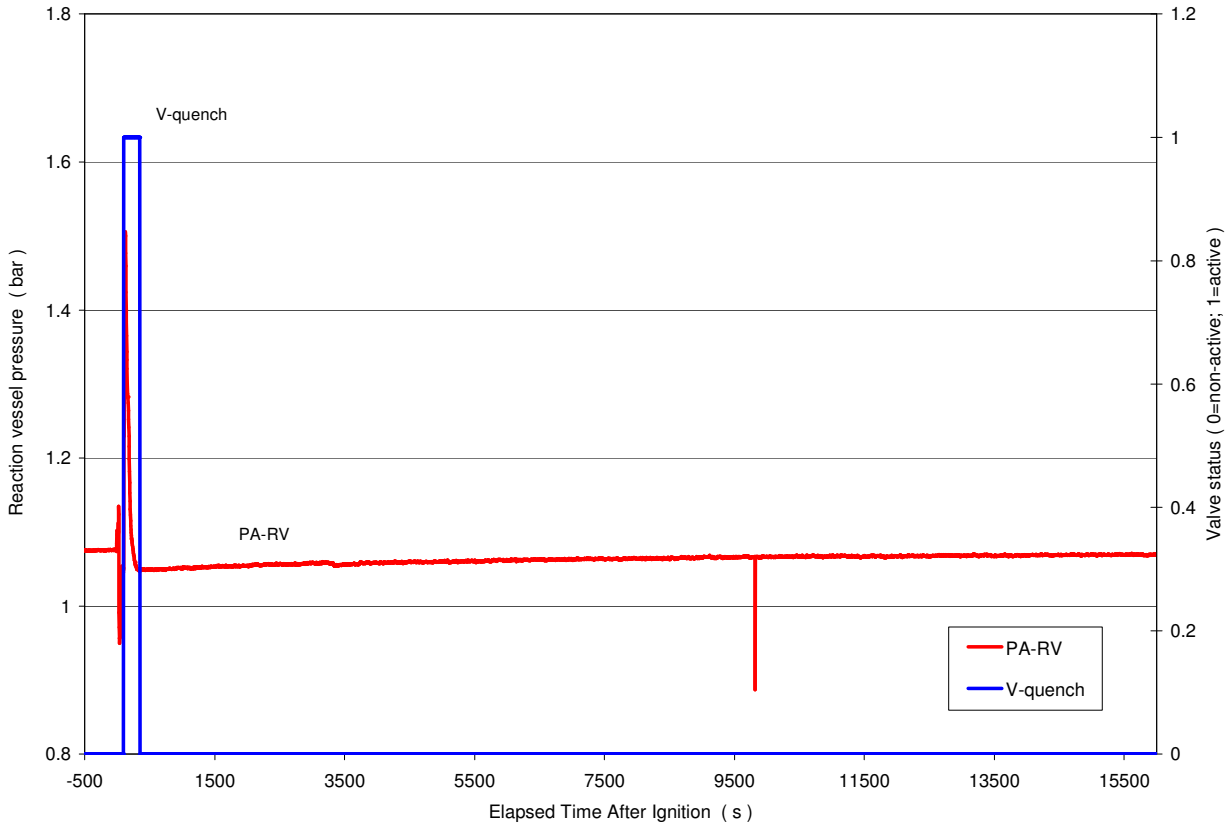

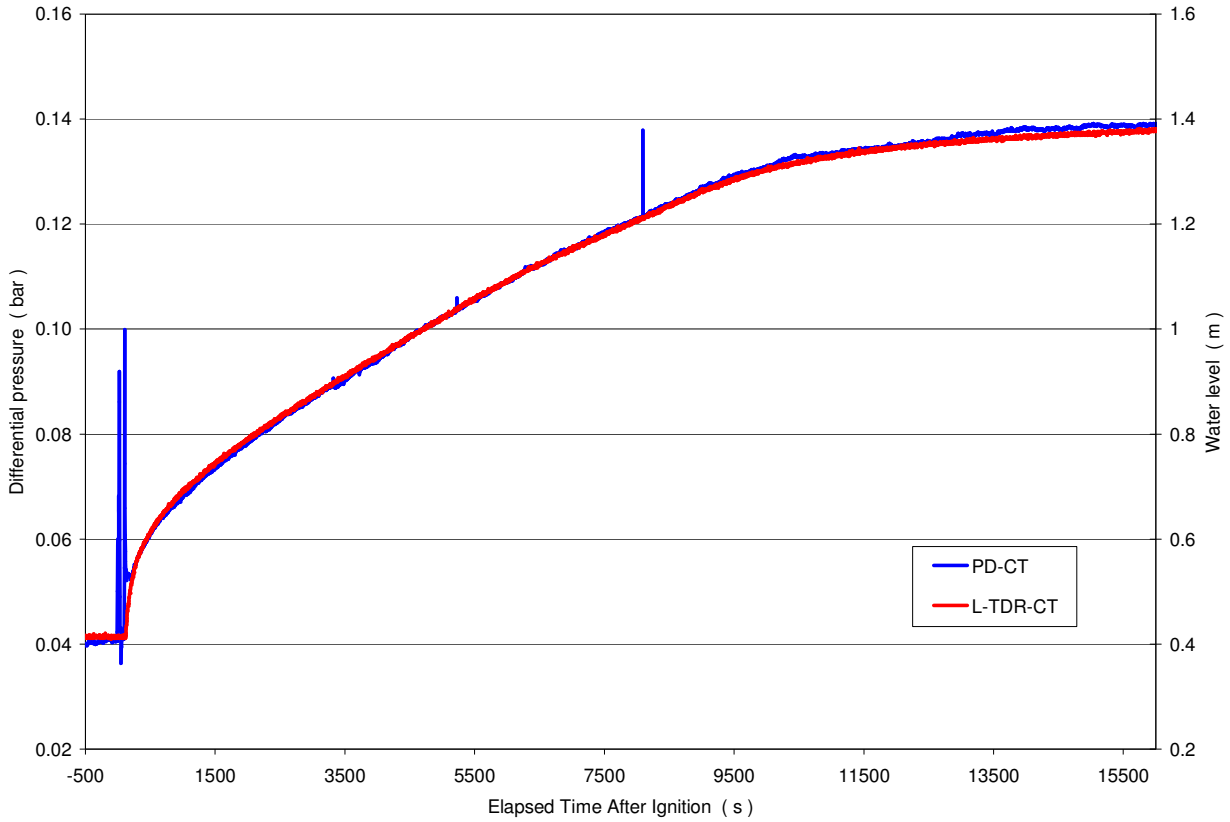

Figure A.7 Condensate tank inventory as measured by ΔP and level sensors.
Figure A.8 Water injection into RV and HX secondary side flow rate.

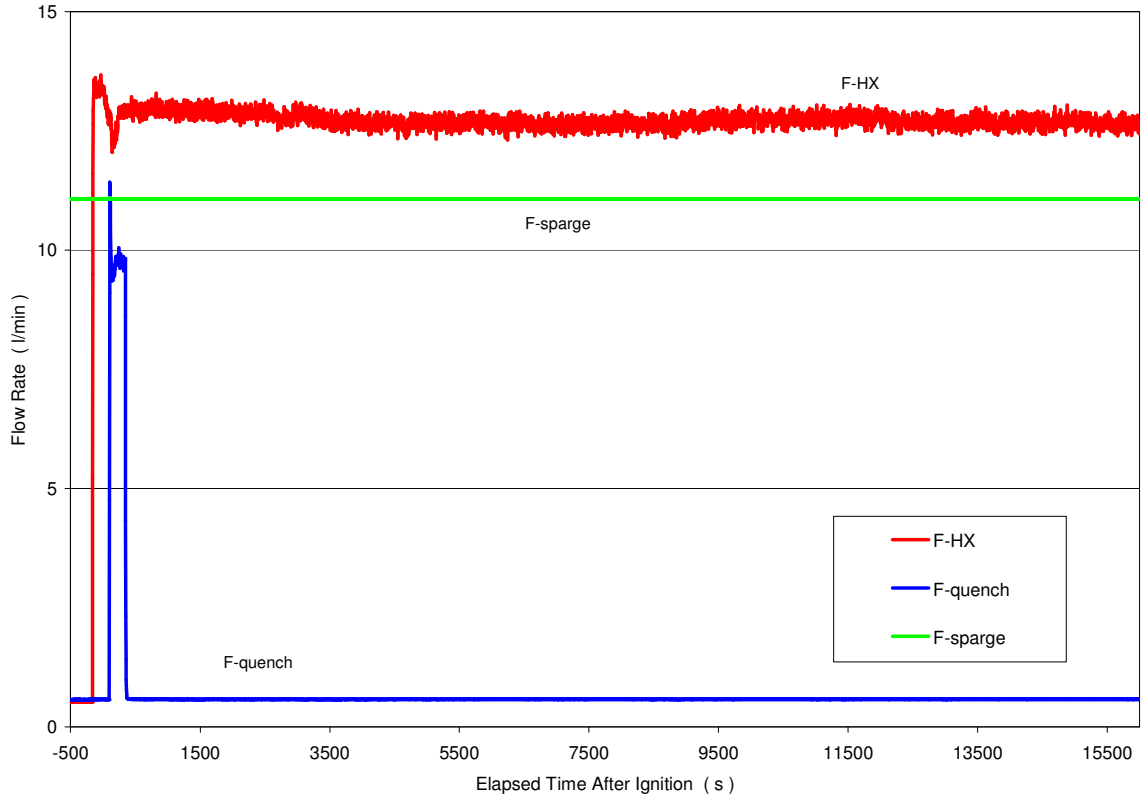

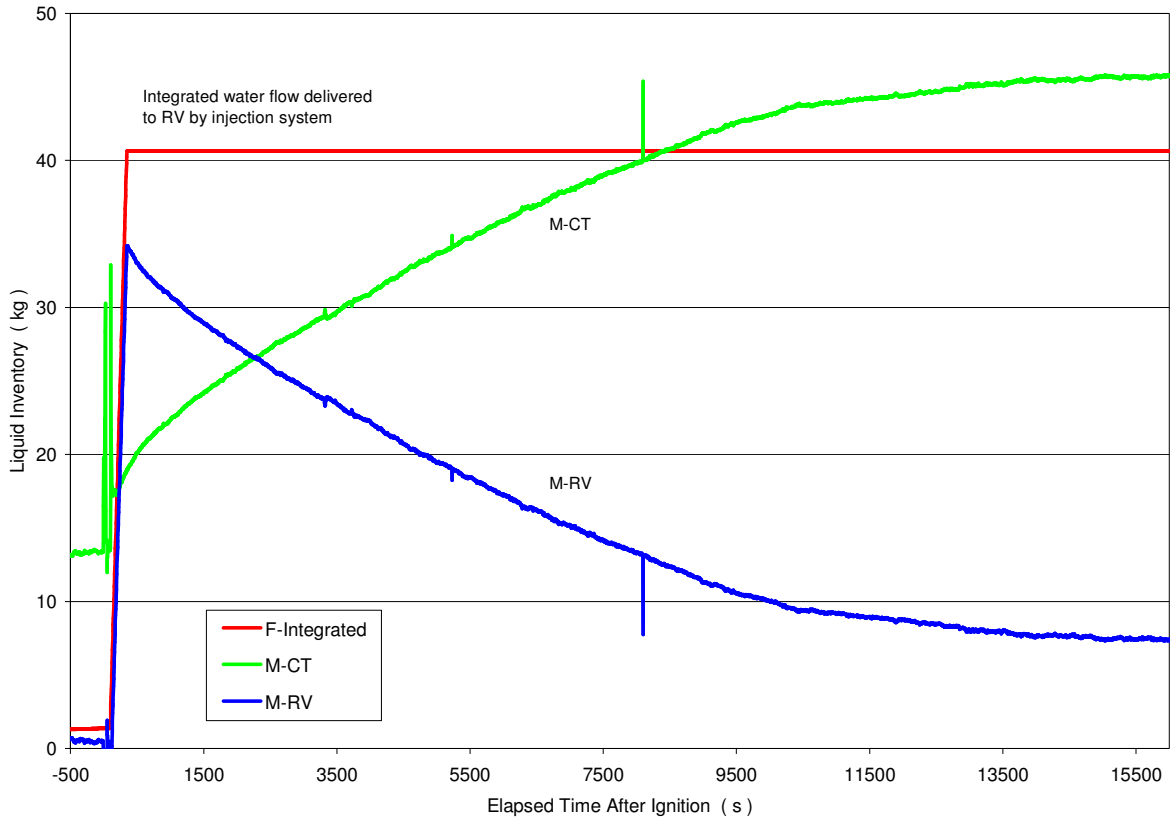

Figure A.9 Integrated quench flow and calculated RV liquid inventory.

Figure A.10 Secondary side fluid temperatures at HX inlet and outlet.

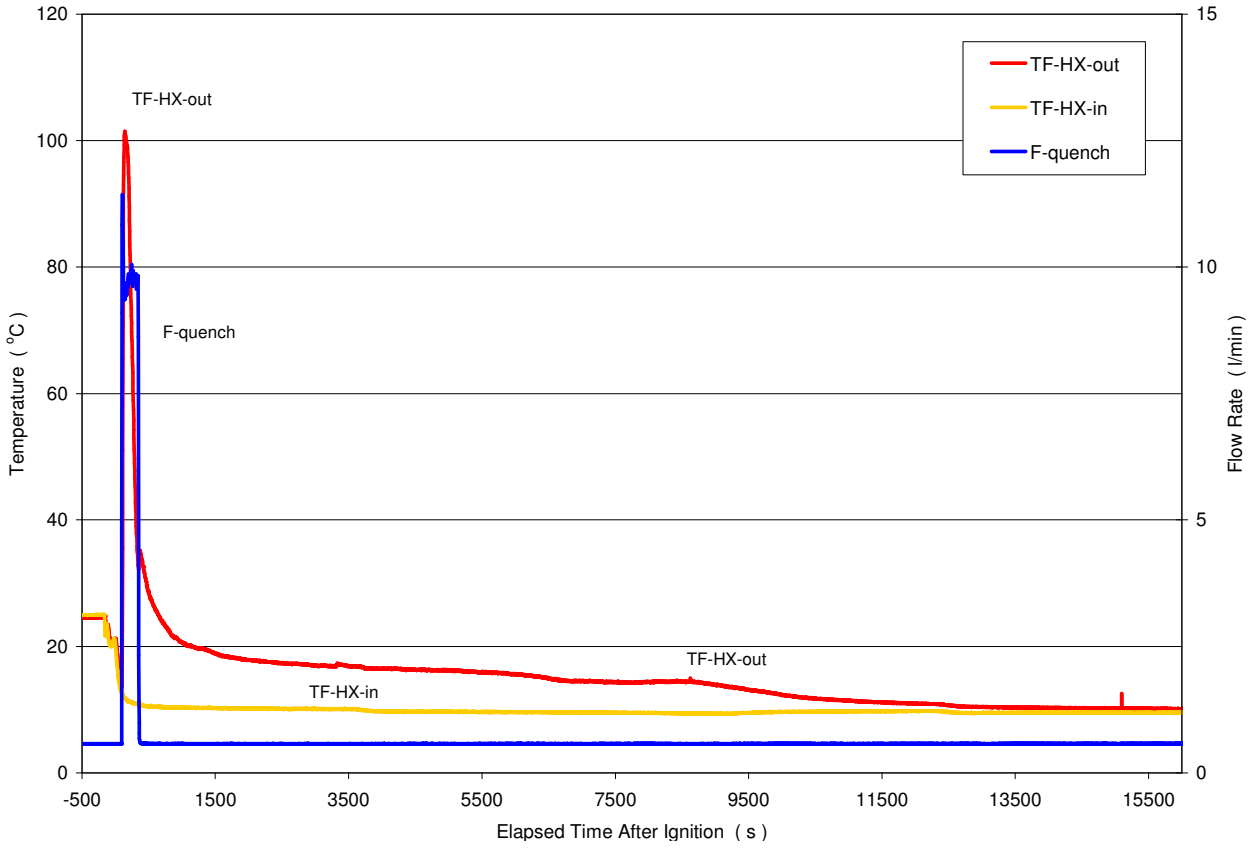

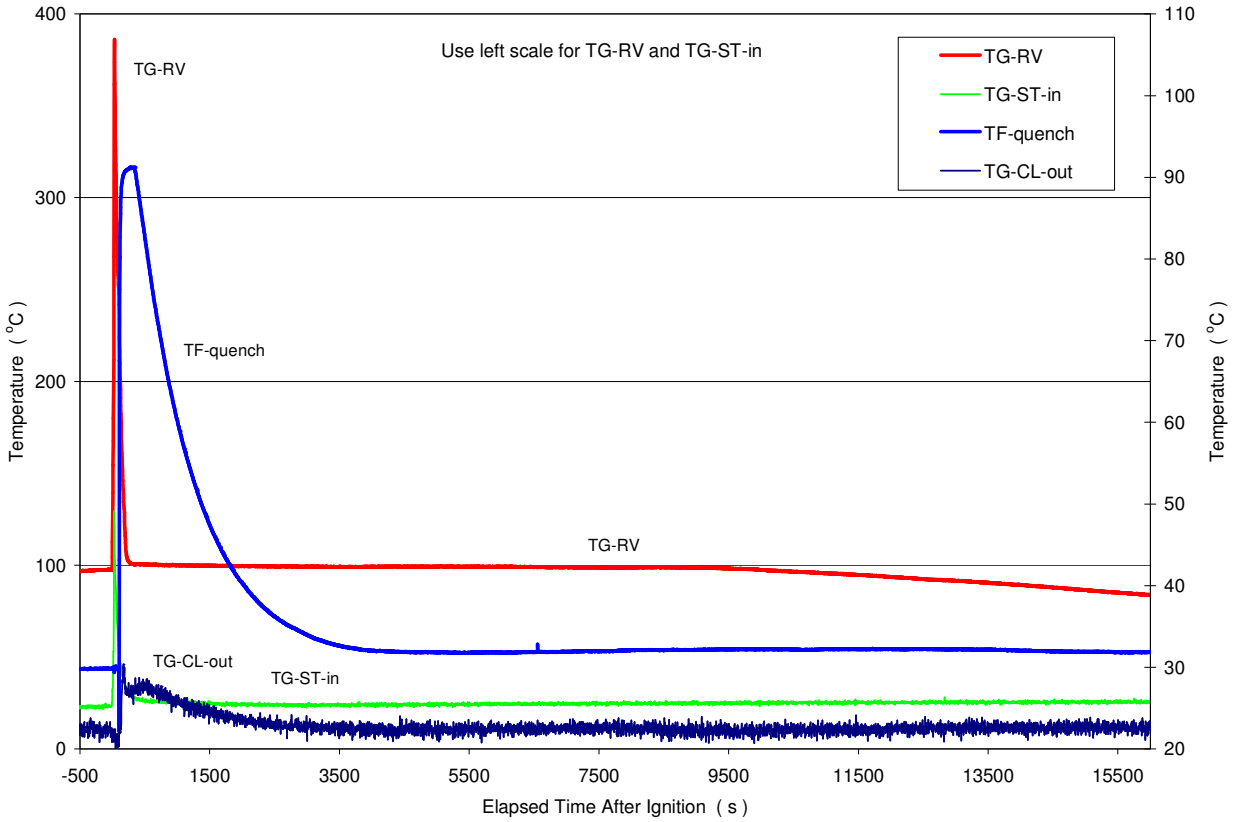

Figure A.11 Miscellaneous gas and fluid temperatures.

Figure A.12 Heat flux through MgO crucible.

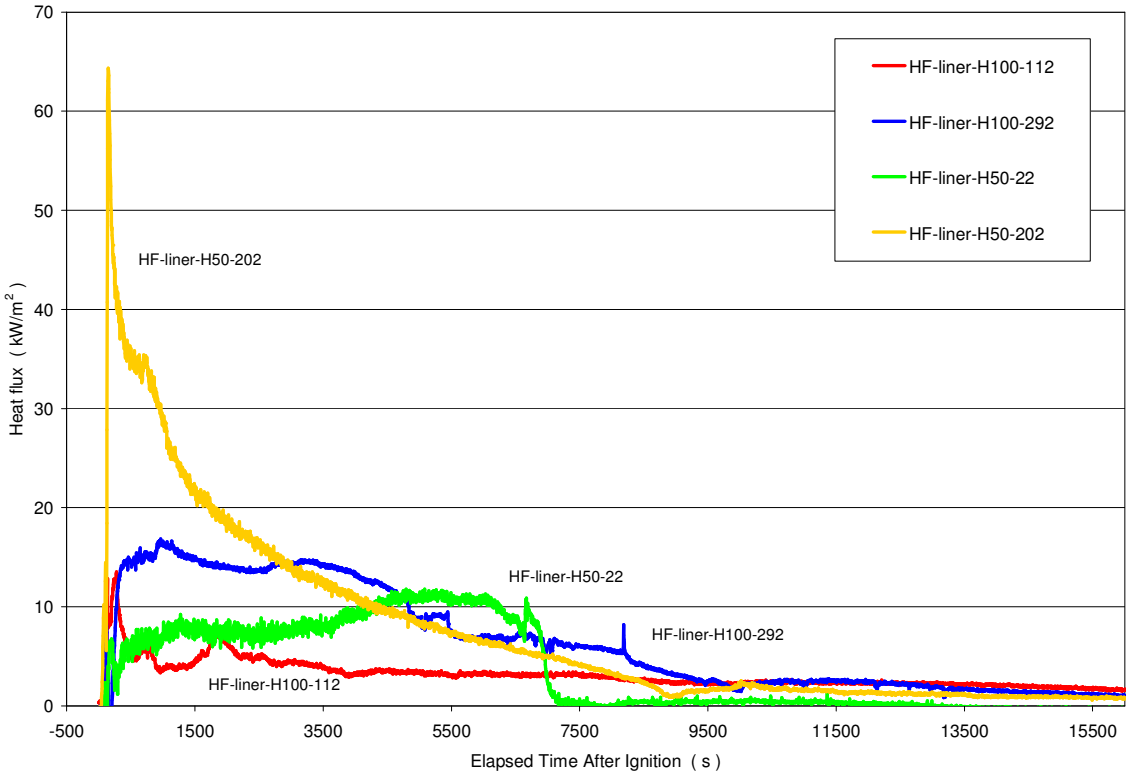

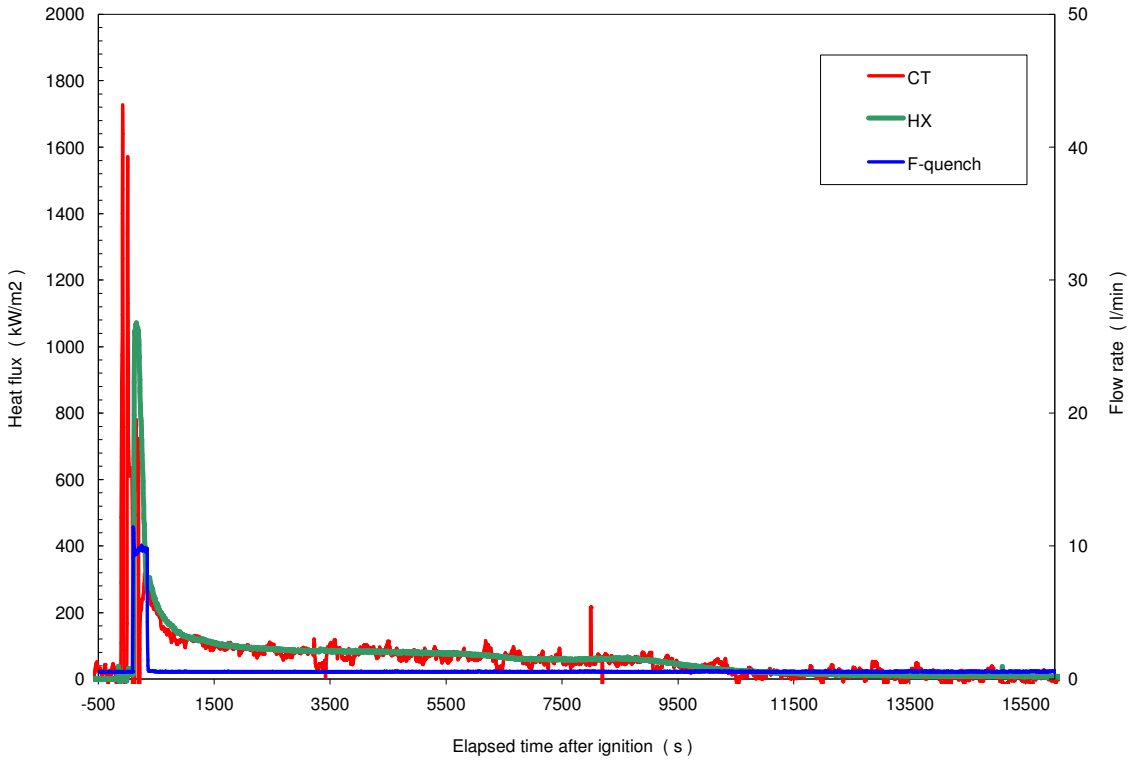

Figure A.13 Energy release from RV, scaled by corium surface area.
Figure A.14 Energy release from RV, scaled by corium surface area (expanded scale).

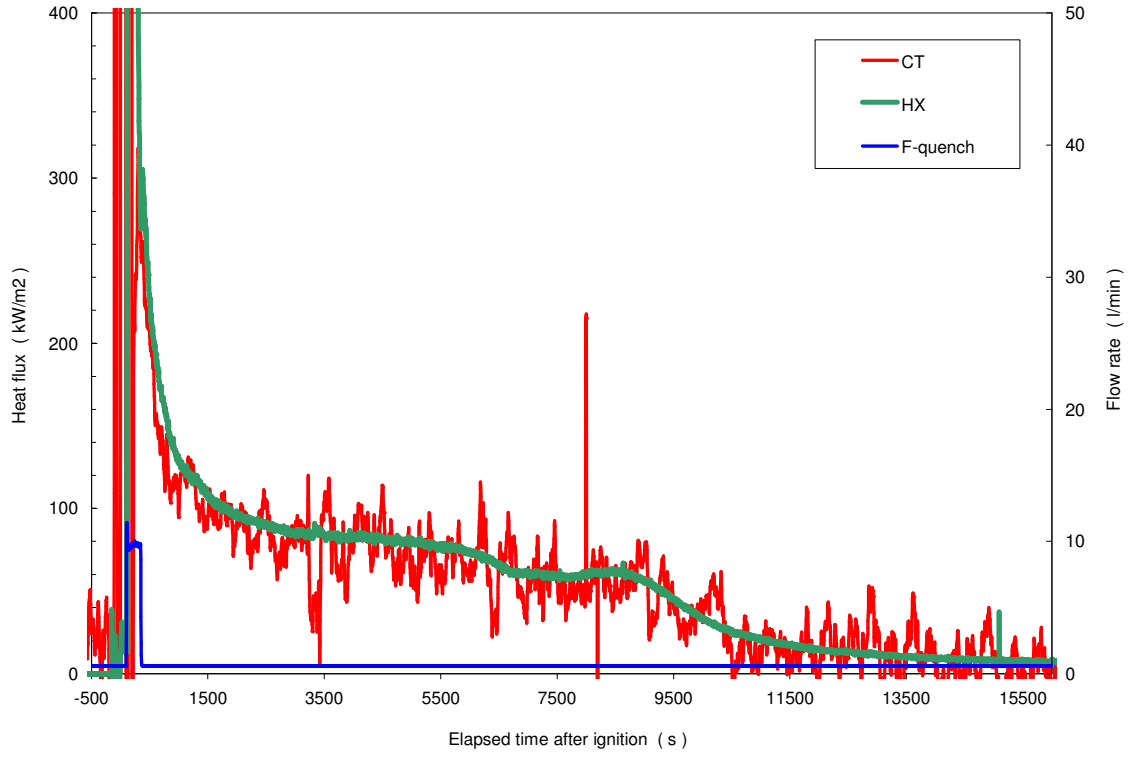

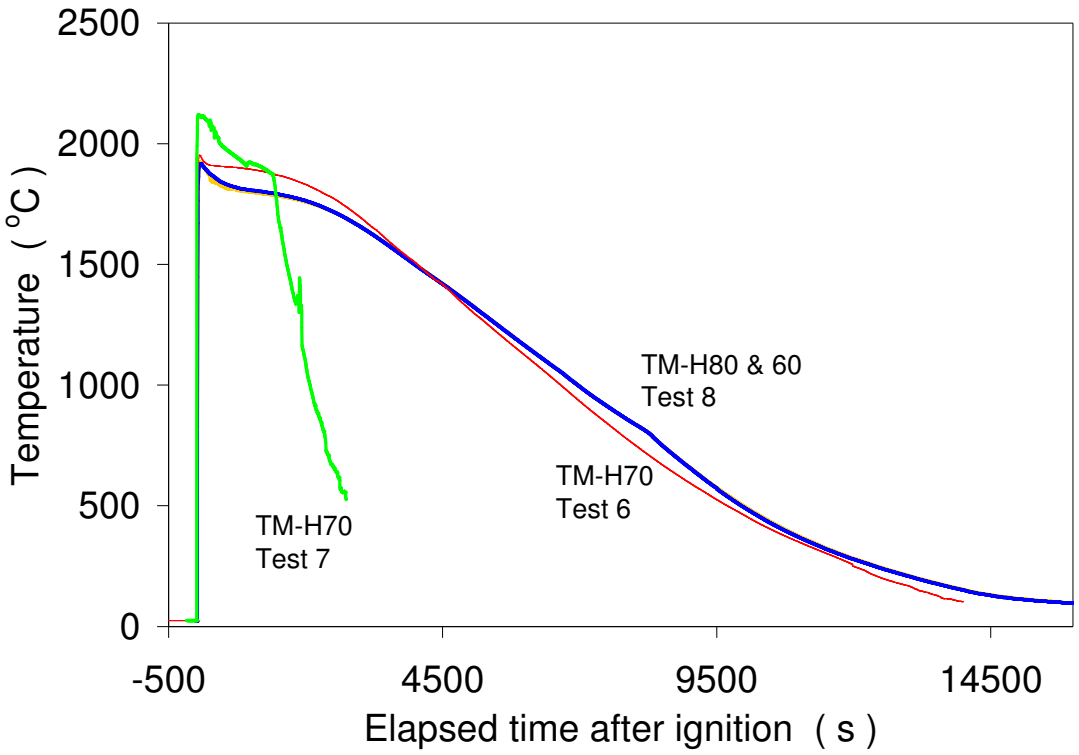

Figure A.15 Comparison of melt temperatures during Tests 6 & 8 (56/23/6/14 wt% UO_2/ZrO_2/Cr/concrete) and Test 7 (64/26/6/4 wt%).

Figure A.16 Cross comparison of measured heat fluxes.

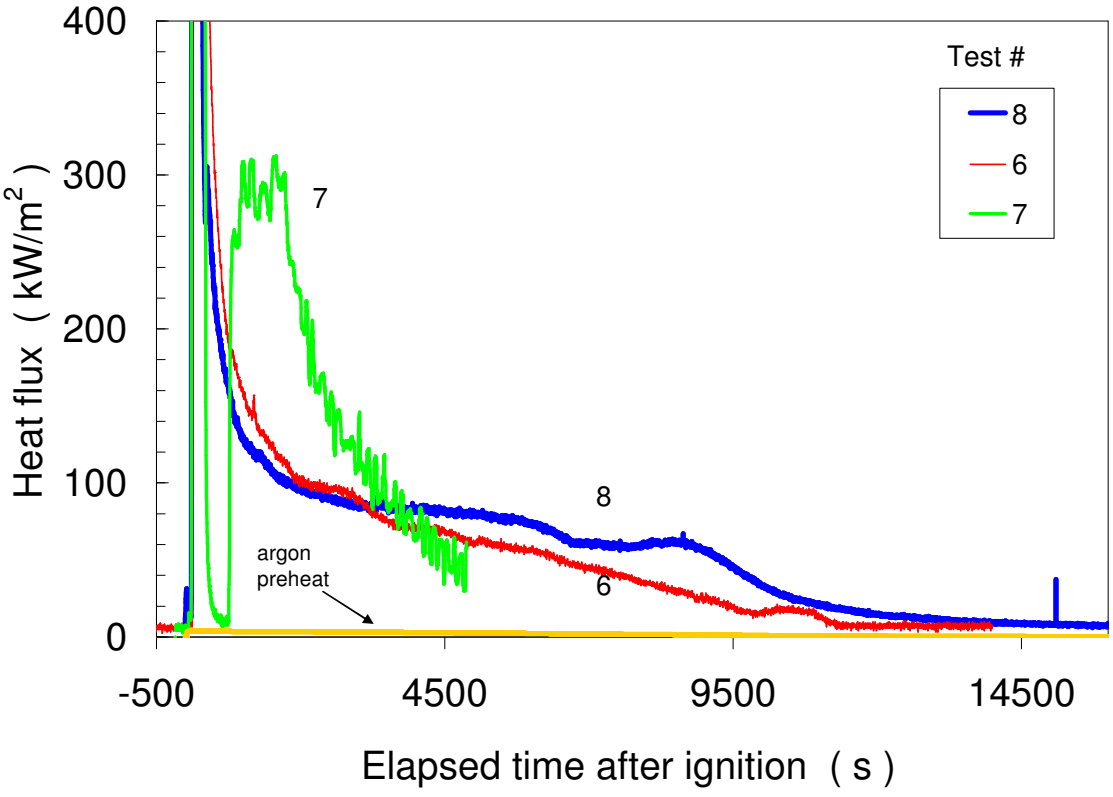

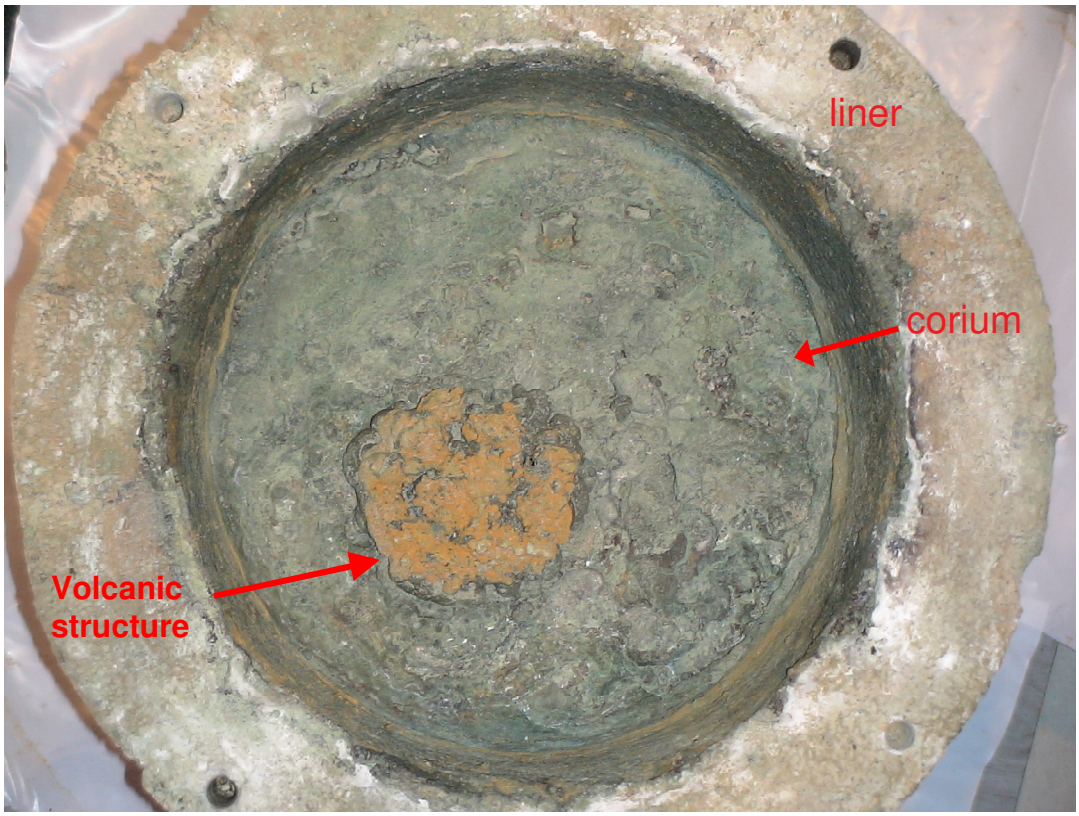

Figure A.17 Top view of corium ingot with liner.

Figure A.18 Bottom view of ingot and liner. Note dimples at locations that were just above capillary outlets.